The requirements of an inner product for real vectors are as follows:

$$\langle a + c,b\rangle = \langle a,b\rangle + \langle c,b\rangle$$

$$\langle \alpha a,b\rangle = \alpha\langle a,b\rangle$$

$$\langle a,a\rangle \geq 0; \quad \langle a,a\rangle = 0 \Longrightarrow a = 0$$

That Eq. (B1) satisfies the first two requirements can be trivially shown. The third requirement is merely the condition that a covariance matrix be positive definite.

Let ξ be the Hilbert space containing the state variable X_n and ζ be the subspace spanned by the measurements $Z_1,\ldots,Z_n$. The difference

$$\delta\hat{X}_{n/n} = X_n - \hat{X}_{n/n}$$

then is contained in that subspace of ξ, not in ζ; i.e., $\xi - \zeta$ is orthogonal to ζ. Therefore, every vector in the subspace $\xi - \zeta$ is orthogonal to every vector in ζ. The vector difference

$$\delta\hat{Z}_n = Z_n - \hat{Z}_n$$

is contained in ζ. Therefore, $\delta\hat{Z}_n$ is the orthogonal to $\delta\hat{X}_{n/n}$ and

$$\langle \delta\hat{X}_{n/n},\ \delta\hat{Z}_n\rangle = X_1{}^T E(\delta\hat{X}_{n/n}\delta\hat{Z}_n{}^T)X_2 = 0 \qquad \text{(B2)}$$

$$E(\delta\hat{X}_{n/n}\delta\hat{Z}_n{}^T) = 0 \qquad \text{(B3)}$$

Substituting Eq. (10) of the text into Eq. (B3) results in

$$E[(\delta\hat{X}_{n/n-1} - K_n\delta\hat{Z}_n{}^T)\delta\hat{Z}_n{}^T] = 0 \qquad \text{(B4)}$$

$$K_n = E(\delta\hat{X}_{n/n-1}\delta\hat{Z}_n{}^T)[E(\delta\hat{Z}_n\delta\hat{Z}_n{}^T)]^{-1} \qquad \text{(B5)}$$

which is the Wiener-Hopf equation.

References

[1] Kalman, R. E., "A New Approach to Linear Filtering and Prediction Problems," *Transactions of the ASME: Journal of Basic Engineering*, Vol. 82, 1960, pp. 35–44.

[2] Bryson, A. E., Jr. and Henrikson, L. J., "Estimation Using Sampled Data Containing Sequentially Correlated Noise," *Journal of Spacecraft and Rockets*, Vol. 5, No. 6, June 1968, pp. 662–665.

[3] Whitcombe, D. W., "Optimum Linear Filtering with Colored Noise," TR-0158(3307-01)-14, June, 1968, The Aerospace Corp., El Segundo, Calif.

[4] Schlee, F. H., Standish, C. J., and Toda, N. F., "Divergence in the Kalman Filter," *AIAA Journal*, Vol. 5, No. 6, June 1967, pp. 1114–1120.

SEPTEMBER 1970 AIAA JOURNAL VOL. 8, NO. 9

A New Treatment of Roll-Pitch Coupling for Ballistic Re-Entry Vehicles

D. A. Price Jr.* and L. E. Ericsson†
Lockheed Missiles & Space Company, Sunnyvale, Calif.

A new source of roll torques which can explain anomalous re-entry motions is presented. Geometric nose asymmetries are shown to cause a normal force component not dependent on angle of attack. The influence of the blunt nose on hypersonic aerodynamics is described with a simple, analytic theory—including effects of entropy gradient and dynamic pressure deficit. This Embedded-Newtonian theory is used to predict load distributions from nose-ablation asymmetries, yielding trim normal forces for high bluntness and trim moments for small bluntness. A powerful coupling with mass asymmetries is thus provided without requiring large trim angles of attack. The resulting motion is predicted with equilibrium trim solutions and verified with digital simulations.

Nomenclature

A = reference area ($\pi d^2/4$), ft²
a = acceleration, g's
b = $\left[C_{N_\alpha}\left(1 - \frac{I_x}{I}\right) - \frac{md^2}{I}(C_{m_q} + C_{m_{\dot{\alpha}}})\right]\frac{\bar{q}A}{mV\omega}$
C_A = axial force coefficient
C_D = drag force coefficient
C_l = roll moment coefficient
C_{l_o} = surface-induced roll moment coefficient
C_{l_g} = roll damping due to grooves/rad
C_{l_f} = roll damping due to friction/rad
C_N = normal force coefficient
$\Delta^i C_{N_o}$ = nose asymmetry induced normal force independent of α
C_m = pitching moment coefficient
C_{m_o} = trim moment coefficient
C_p = pressure coefficient
C_{p_o} = blast wave pressure coefficient
$C_{p\text{Newt}}$ = Newtonian pressure coefficient
d = base diameter, ft
I = pitch moment of inertia, slug-ft²
I_x = roll moment of inertia, slug-ft²
i = $(-1)^{1/2}$
L_N = total surface recession at stagnation point, ft
L_o = sharp cone length, ft
m = vehicle mass, slugs
p = spin rate, rad/sec
$\bar{q}$ = dynamic pressure ($\rho V^2/2$), lb/ft²
$\bar{q}_l$ = local dynamic pressure, lb/ft²
r = radial distance from center line, ft
R = complex angle-of-attack moduli
t = time, sec

Presented as Paper 69-101 at the AIAA 7th Aerospace Sciences Meeting, New York, January 20–22, 1969; submitted February 17, 1969; revision received March 2, 1970.

* Staff Scientist, Engineering Technology.
† Senior Staff Engineer, Engineering Technology. Associate Fellow AIAA.

V = velocity, fps
$\Delta\bar{x}$ = center of gravity location, ft (see inset, Fig. 6)
x_M = static margin, ft
x,y,z = axial, lateral, and vertical coordinates (see Figs. 1 and 20)
α = angle of attack, rad or deg
β = angle of side slip, rad or deg
Γ = orientation of r_G, rad or deg (see Fig. 9)
δ = equivalent fin cant angle of ablation grooves, rad or deg
Δ = difference or increment
ω_o = $[\omega^2 + (pI_x/2I)^2]^{1/2}$
$\Delta\omega$ = $p(1 - I_x/2I)$
ζ = complex angle-of-attack, rad or deg (see Fig. 8)
ω = aerodynamic frequency $[-C_{m_\alpha}\bar{q}Ad/I]^{1/2}$, rad/sec
θ = surface slope, rad or deg (see Fig. 2)
ϕ = azimuth angle, rad or deg (see Fig. 5)
ψ = phase shift between α_{TRIM} and α_{ST}, rad or deg
ρ = air density, slugs/ft^3
λ = orientation of α_{ST}, rad or deg (see Fig. 9)
τ = time lapse since formation of ablation grooves, sec

Subscripts

B = base
c = cone
c.g. or G = center of gravity
F = friction
N = nose
R = resultant
SH = shock
ST = trim at $p = 0$
T = peak trim magnitude
TRIM = trim at $p \neq 0$

Superscripts

$\cdot$ = $\partial/\partial t$
i = induced; e.g., $\Delta^i C_N$ = nose asymmetry-induced incremental normal force

Derivatives

$$C_{N_\alpha} = \frac{\partial C_N}{\partial \alpha}; \quad C_{l_\delta} = \frac{\partial C_l}{\partial \delta}; \quad C_{l_p} = \frac{\partial C_l}{\partial (pd/2V)}$$

I. Introduction

PREVIOUS treatments of ballistic re-entry body dynamics have proceeded from the assumption of a symmetric spinning vehicle with small longitudinal trim asymmetries and lateral mass asymmetries.[1–5] The resulting roll-pitch coupling, with the normal force limited to the form $C_N = C_{N_\alpha}\alpha$, was unable to fully explain the roll behavior observed in flight test. The difference between the roll torques predicted from center of gravity offset coupling with a normal force proportional to angle of attack, and the torque required to explain flight data was attributed to ablation-induced roll moments or simply lumped under an unexplained roll moment coefficient (C_{l_o}). However, this pure rolling moment had often opposite direction to that expected and displayed disconcerting changes in direction and magnitude.

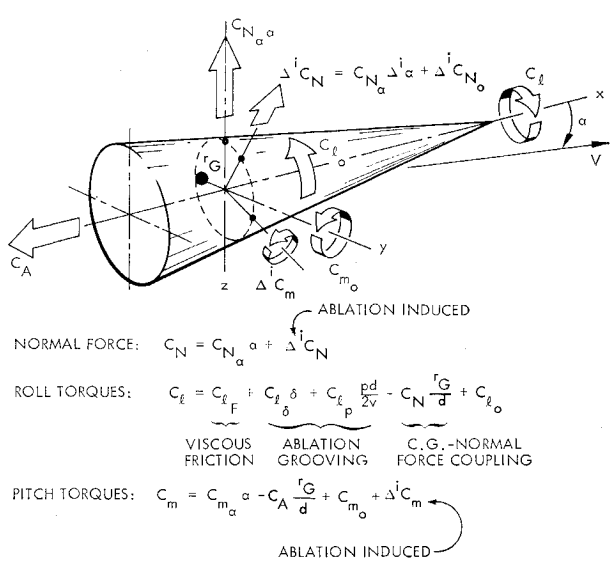

Fig. 1 Aerodynamic characteristics formulation with ablation-induced asymmetries.

In the new treatment presented here, the previously used definition of small asymmetries is re-examined and found unrealistic for slender bodies with blunted nose shapes. Hence, the aerodynamic characteristics are formulated in a more general manner, as illustrated in Fig. 1. An additional normal force component ($\Delta^i C_{N_o}$) which is independent of angle of attack is introduced to account for unsymmetrical nose ablation. The pitching moment includes the component $\Delta^i C_m$ from the nose asymmetry. The preflight moment asymmetry is denoted by C_{m_o} as before. The $\Delta^i C_{N_o}$ and $\Delta^i C_m$ components will not, in general, lie in the resultant angle-of-attack plane, as depicted in Fig. 1. Roll torques are described by a viscous friction term (C_{l_F}), an ablation-grooving term $C_{l_\delta}\delta + C_{l_p}pd/2V$, analogous to the canted-fin driving and damping moments,[4] and by the c.g.—normal force coupling which now includes the nose asymmetry normal force component $\Delta^i C_{N_o}$. It is readily apparent that this force can provide a powerful coupling with mass asymmetries resulting in significant roll rate changes without requiring unreasonably large trim angles of attack.

II. Nose-Induced Aerodynamic Effects

With the introduction of blunted nose shapes, the simple Newtonian theory could no longer be used for prediction of hypersonic aerodynamics. Instead, complicated numerical schemes had to be used, such as the method of characteristics. This step from the simple Newtonian theory was a severe setback for preliminary design as it destroyed the design engineer's intuitive feel for how the aerodynamics would change with geometry. It also made it more difficult to achieve a comprehensive understanding of the over-all motion dynamics of a re-entering high-performance entry vehicle, the ambitious goal of the present paper. Thanks to Seiff,[6,7] who first pointed out the road to an analytic extension of the Newtonian theory, we have been able to develop an Embedded-Newtonian theory, which is almost as simple as the pure Newtonian theory.[8–10]

The Embedded-Newtonian flowfield described by Seiff[7] is shown in Fig. 2. The pressure on the surface element embedded in the "entropy wake" generated by the blunt nose can be expressed as follows:

$$C_p = C_{p_o} + C_{p_{Newt}}(\bar{q}_l/\bar{q}) \tag{1}$$

C_{p_o} is the static pressure in absence of aft body, the blast wave pressure. The dynamic pressure ratio is a function of radial location in the entropy wake and, using similarity concepts, it can be expressed as follows[9,10]:

$$\bar{q}_l/\bar{q} = f(r/r_{SH}) \tag{2}$$

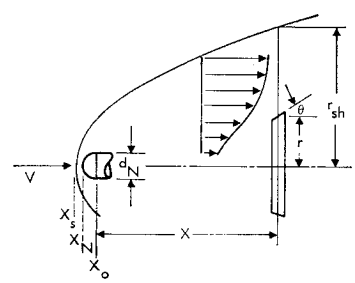

Fig. 2 Embedded-Newtonian flowfield.

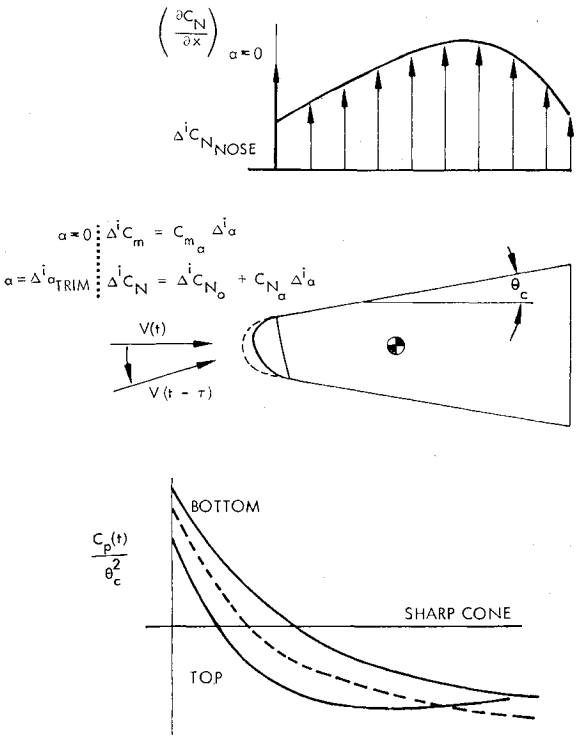

Fig. 3 Effects of nose asymmetries on very blunt cones.

As C_{p_o} is practically constant across the inner 50% of the entropy wake, the flare forces are determined by $f(r/r_{SH})$ and $C_{p_{Newt}}$. A simple analytic theory can be developed that does not only take the dynamic pressure deficit into account, but also accounts for the effects of entropy gradient and time lag.[8–10]

On a slender blunted cone the "bucket" in the pressure distribution is a manifestation of the entropy wake effect described in the Embedded-Newtonian theory.[8] A simple analytic treatment of nose bluntness effects on cone aerodynamics can be derived[10] that gives results that agree well with available experimental data.

From the preceding discussion it is obvious that a blunted nose induces large changes of the aft body loads. For small nose bluntness these load changes outweigh the effect of the nose load itself. Consequently, one can expect nose asymmetry to induce appreciable trim loads on the aft body, in addition to the nose load change itself (Figs. 3 and 4). On a highly blunted cone a positive load distribution would result from nose oblateness produced by earlier ablation at a certain trim angle (Fig. 3). As a result the vehicle will at a later time in flight have a composite aerodynamic asymmetry made up by a normal force increment $\Delta^i C_{N_o}$, which is independent of the current (instantaneous) angle of attack, in addition to the trim angle-of-attack dependent force, $C_{N_\alpha}\alpha_{TRIM}$. The important point is that $\Delta^i C_{N_o}$ may, and most likely will, be located in a plane different from the plane of the trim angle α_{TRIM} existing at a later time in the re-entry trajectory. For a less blunt vehicle, on the other hand, the loads induced by the nose asymmetry will more closely result in a pure trim effect, i.e., $\Delta^i C_{N_o} \approx 0$ (Fig. 4).

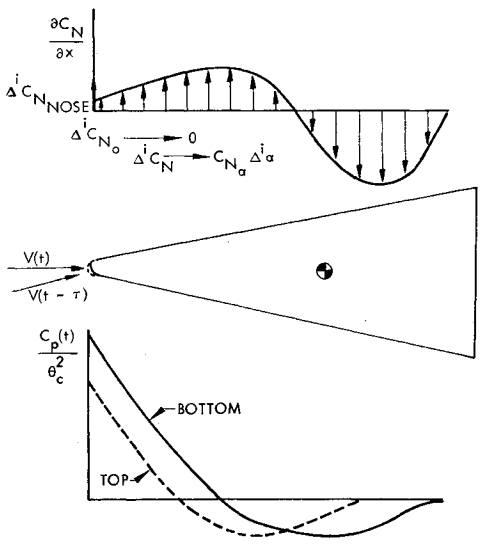

Fig. 4 Effects of nose asymmetries on moderately blunt cones.

When a spherically tipped cone is blunted through ablation at trim angle of attack the asymmetric shape sketched in Fig. 5 may be visualized as a possible result; the "effective" spherical nose radius deviates from the mean radius r_N by the amount $\Delta r_N \sin\phi$, and the start of the conic frustum varies around the circumference by the corresponding amount $\Delta R_N \sin\phi \cot\theta_c$. This is obviously not the true ablated nose shape. Rather, it is intended to represent the mean nose asymmetry by an effective pseudo-spherical deformation, thereby allowing easy computation of the loading induced on the conical frustum by the nose asymmetry. A blunted cone with half cone angle $\theta = 5.73°$ (0.1 rad) induces the loads shown in Fig. 6. At 8% nose bluntness, when the sharp cone pressure is reached at the trailing edge, the induced normal force dips down to zero, but increases thereafter sharply with increasing nose bluntness. The figure shows that the induced pitching moment may be zero for large nose bluntness. That is, the net effect of the loads induced on the conical shell can be a pure normal force without any trimming moment.

Adding the local nose load itself, computed by modified Newtonian theory ($C_{p_{max}} = 1.8$), gives the total normal force shown in Fig. 7. Even at 20% nose bluntness, the normal force induced on the conical frustum is as large as the local nose normal force itself! If the nose asymmetry were 10%, i.e., $\Delta r_N/r_N = 0.10$, a 30% blunt cone with $\theta_c = 0.1$ rad would have a total normal force due to nose asymmetry at $\alpha = 0$ which is equal to the normal force generated by an angle of attack of 0.34°. Thus, it does not take much of a nose asymmetry to generate a normal force at zero angle of attack which is of the magnitude needed to explain some of the anomalous spin behaviors that have been observed in re-entry flights of blunted slender cones.

III. Motion Behavior

Previous studies[1–5] have shown that spin rate changes arise primarily from coupling between lateral mass asymmetries and steady trim forces. The rationale behind this conclusion

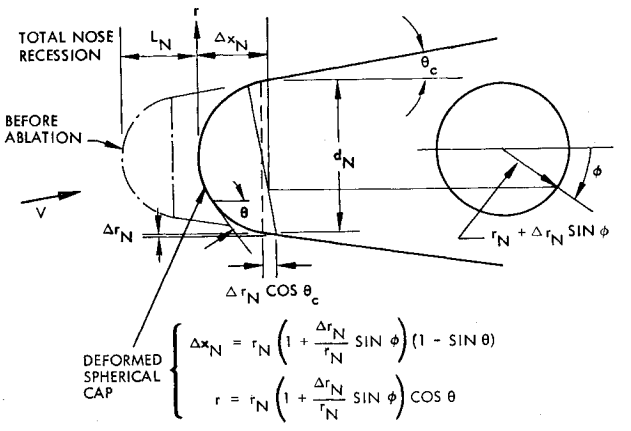

Fig. 5 Postulated deformation through ablation.

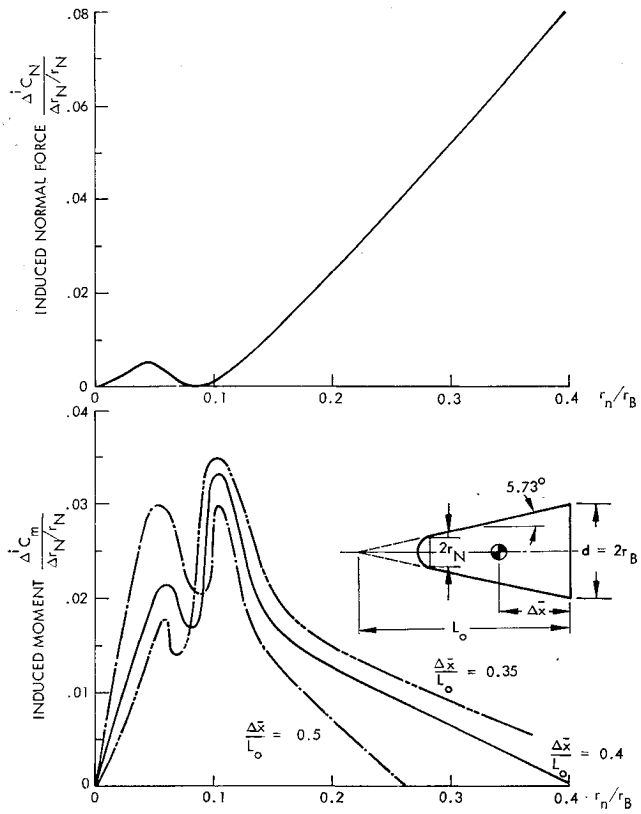

Fig. 6 Loads induced on conical frustums per unit nose asymmetry at $\alpha = 0$.

is illustrated in Fig. 8 for a body fixed-reference axis system. The resultant complex angle of attack $\zeta = \beta + i\alpha$ is described by two time-varying, damped vectors, R_1 and R_2, rotating at different rates, $\omega_o - \Delta\omega$ and $\omega_o + \Delta\omega$, respectively, about the trim component α_{TRIM}. For positive spin rate p, R_2 always rotates faster than R_1 in a counterclockwise direction, whereas R_1 changes its direction of rotation depending on the relative magnitude of ω_o and $\Delta\omega$. The α_{TRIM} orientation and magnitude vary with proximity to resonance; $\omega = p(1 - I_x/I)$. With a c.g. displaced from the geometric (or aerodynamic) centerline, a roll torque is generated whose magnitude and direction depend upon the orientation and

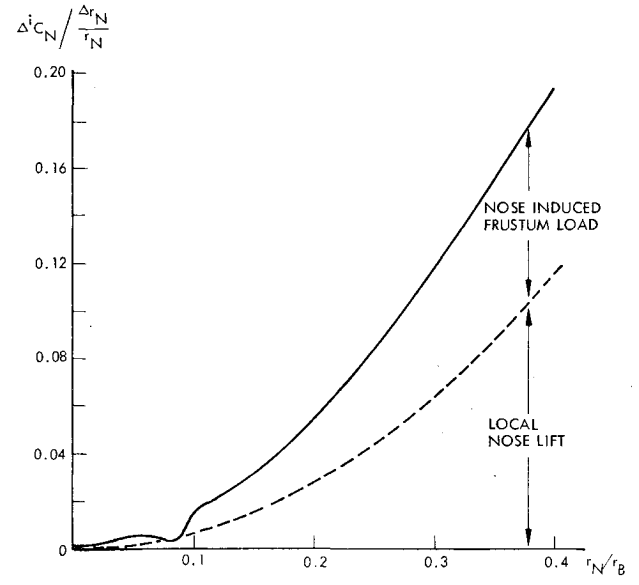

Fig. 7 Total normal force produced per unit nose asymmetry at $\alpha = 0$.

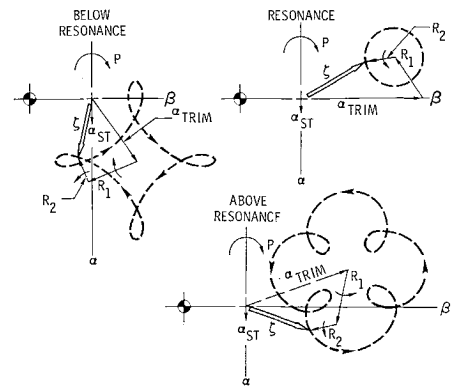

Fig. 8 Total angle of attack.

magnitude of ζ. Since R_1 and R_2 prescribe motions about the trim component, the average roll torque is generated by α_{TRIM}. Hence, in the subsequent development, only the trim angle of attack will be considered.

The variation of α_{TRIM} magnitude and orientation with proximity to resonance p/ω is depicted in Fig. 9 for a constant environment ω. With increasing p/ω, α_{TRIM} rotates counterclockwise to $\psi \approx -90°$ at resonance and grows to a peak magnitude α_T limited only by the aerodynamic damping factor b. A further increase of p/ω above resonance rotates and decreases α_{TRIM} to 0 and ψ toward $-180°$. Note that large α_{TRIM} is maintained for $\Delta\psi \approx \pm 45°$ about resonance. With changing environment, the peak amplification $\alpha_T/\alpha_{\text{ST}}$ will change with the damping factor b, whereas the orientation is affected only slightly. Thus, if significant undamping occurs due to unsteady aerodynamic and ablation effects,[8–11] the trim will exhibit a growth similar to the usual dynamic motion instability.

The $\Delta^i C_m$ from an ablation induced nose asymmetry will contribute directly to the preflight trim moment C_{m_o} to produce the resultant static trim α_{ST} shown in Fig. 9. The effect will be to amplify the motion behavior expected for the preflight anomalies rather than to change its character.

The arrangement of symmetries in Fig. 9 will produce a roll moment which changes direction as p and ω vary. For example, if $-\psi > (\lambda - \Gamma)$, the c.g.-normal force coupling will yield a spin-up roll moment. When the $C_{N\text{TRIM}}$ is aligned with the c.g., the roll moment is zero. This particular arrangement represents an unstable roll trim since any change of ω will cause p to change in the opposite direction, increasing or decreasing away from the trim value.

To this situation we now add the previously neglected normal force component $\Delta^i C_{N_o}$. Since $\Delta^i C_{N_o}$ results from a body fixed geometric asymmetry, its orientation λ_o is independent of the instantaneous value of p/ω. Hence, a constant roll torque results, which is not directly related to the current trim angle of attack.

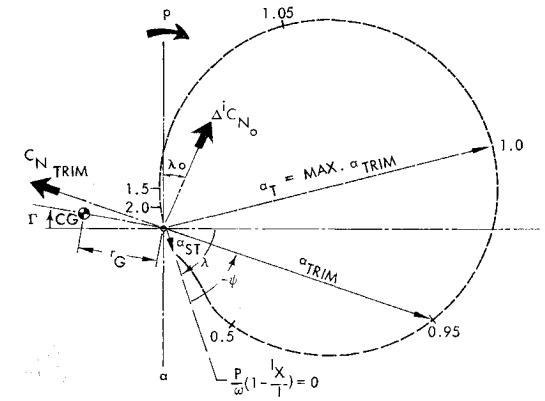

Fig. 9 Rolling trim response.

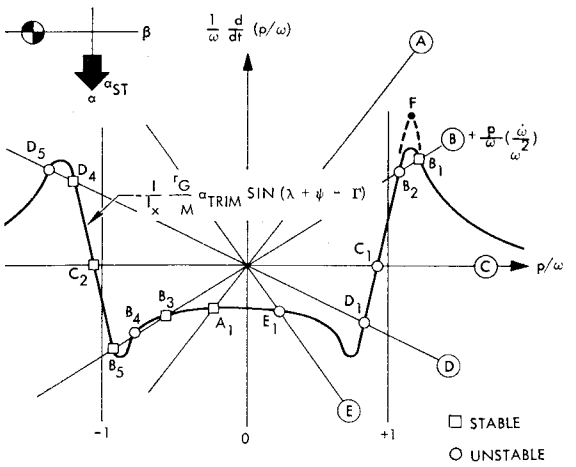

Fig. 10 Variation of roll trim with environment for c.g.-α_{TRIM} coupling.

The roll torque equation now takes the form

$$I_x\dot p = \left[-\frac{r_G}{d}\Delta^i C_{N_o}\cos(\lambda_0-\Gamma) - \frac{r_G}{d}C_{N_\alpha}\alpha_{TRIM}\times \sin(\lambda+\psi-\Gamma) + C_{l_f}\frac{pd}{2V} + C_{l_\delta}\delta + C_{l_g}\frac{pd}{2V}\right]\bar q A d \quad (3)$$

where $\delta \equiv (pd/2V)_{(t-\tau)}$.

The ablation grooving effects are treated as those of equivalent canted fins formed at time $(t-\tau)$. The viscous friction term represents the moment arising from the circumferential component of the surface shear with spin. Note that all the quantities in Eq. (3) are specified throughout the trajectory for a given spin rate. Introducing the static stability C_{m_α} and rearranging Eq. (3) yields the roll acceleration

$$\dot p = -\frac{I}{I_x}\left[\frac{\Delta^i C_{N_o}}{C_{N_\alpha}}\frac{r_G}{x_M}\cos(\lambda_0-\Gamma) + \frac{r_G}{x_M}\alpha_{TRIM}\sin(\lambda+\psi-\Gamma) - \frac{C_{l_f}}{C_{N_\alpha}}\frac{d}{x_M}\frac{pd}{2V} - \frac{C_{l_\delta}\delta}{C_{N_\alpha}}\frac{d}{x_M} - \frac{C_{l_g}}{C_{N_\alpha}}\frac{d}{x_M}\frac{pd}{2V}\right]\omega^2 \quad (4)$$

For a slowly varying environment, the steady-state spin rate ($\dot p = 0$) occurs when the bracketed terms become zero. However, the proximity of the spin rate to resonance is more descriptive of the motion behavior. To maintain p/ω constant requires that

$$(d/dt)(p/\omega) = \dot p/\omega - p(\dot\omega/\omega^2) = 0 \quad (5)$$

Equation (5) represents a generalization of the criterion for roll resonance described by Mitgotsky[5] which is applicable for any spin rate with variable environment ω. Applying Eq. (5) to the roll acceleration, Eq. (4), provides

$$\frac{1}{\omega}\frac{d}{dt}\left(\frac{p}{\omega}\right) = -\frac{I}{I_x}\left[\frac{\Delta^i C_{N_o}}{C_{N_\alpha}}\frac{r_G}{x_M}\cos(\lambda_o-\Gamma) + \frac{r_G}{x_M}\alpha_{TRIM}\sin(\lambda+\psi-\Gamma) - \frac{C_{l_o}d}{C_{N_\alpha}x_M}\right] - \frac{p}{\omega}\left(\frac{\dot\omega}{\omega^2}\right) \quad (6)$$

where, for brevity,

$$C_{l_o} = C_{l_\delta}\delta + C_{l_p}(pd/2V)$$

$$C_{l_p} = C_{l_f} + C_{l_g}$$

Hence, when the spin rate parameter becomes zero, a roll trim is defined. The roll trim solutions will be developed graphically in order to illustrate the mechanisms of the roll coupling more clearly.

Roll Trim for ($r_G\alpha_{TRIM}$) Coupling

The coupling for a vehicle with moment and mass asymmetry only is depicted in Fig. 10 for an orthogonal arrangement of the c.g. offset and static trim, as depicted by the inset sketch. This relative orientation yields a negative roll moment below resonance. The variation of the spin rate parameter is illustrated in terms of the trim parameter

$$-(r_G/x_M)(I/I_x)\alpha_{TRIM}\sin(\lambda+\psi-\Gamma)$$

and the negative of the pitch rate parameter $-p/\omega(\dot\omega/\omega^2)$.

The amplification and orientation change of the resonant α_{TRIM} with respect to the c.g. offset yields the rapid change of this asymmetry coupling term in the vicinity of resonance. For a constant environment ($\dot\omega = 0$), two roll trim solutions or roots C_1 and C_2 near resonance are possible. The only stable trim point is C_2 at negative roll rate. For a given time in the trajectory, the pitch rate parameter yields an inclined straight line through the origin. The intersections (e.g., A_1) of the curves then represent possible roll trim solutions.

The variation of these roll trim solutions can be traced for a changing environment by examining the effect of ω on the shape of the curves in Fig. 10. The primary change occurs in the slope of the $p/\omega(\dot\omega/\omega^2)$ lines labeled A through E. The change of the $r_G\alpha_{TRIM}$ contour is much smaller (omitted for clarity) and affects the magnitude of the peak as noted by point F. At high altitude, a single stable root A_1 exists with a negative spin rate. With decreasing altitude (decreasing $\dot\omega/\omega^2$), multiple roots appear as depicted by line B for which points B_1, B_3, and B_5 are stable, and points B_2 and B_4 are unstable. At peak dynamic pressure (line C), the constant environment solutions apply. Similar roll trims can be defined for the remainder of the trajectory (e.g., lines D and E).

The steady roll rates corresponding to these roll trim solutions can then be traced out for the full trajectory, as illustrated in Fig. 11. The example solutions (A–E) of Fig. 10 are included for reference. The variations of the trimmed roll rates are compared with the aerodynamic pitch frequency ω. Stable trims are indicated by the solid curves and the unstable roots by the dashed curves.

The roll rate behavior of a vehicle with sufficiently large asymmetries can now be predicted as illustrated by the shaded lines in Fig. 11. For example, if the initial spin rate were zero, the spin rate will follow roots A_1, B_3 to B'_3. Because the roll torque is negative beyond B'_3, the roll rate will jump to B_5 and thence follow C_2 to D_4. After time D'_4 the

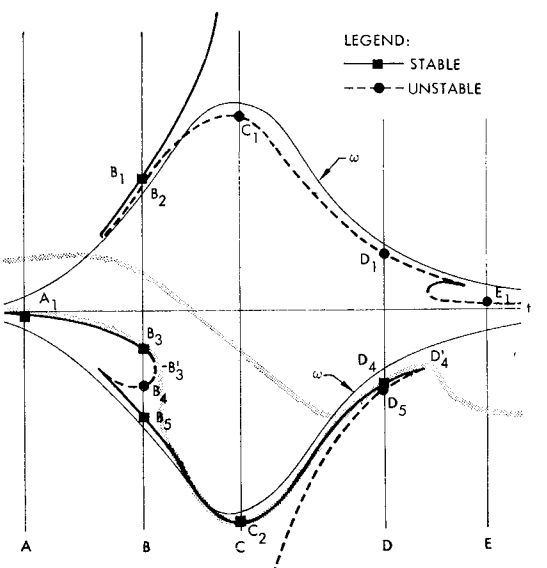

Fig. 11 Roll trim histories for c.g.-α_{TRIM} coupling.

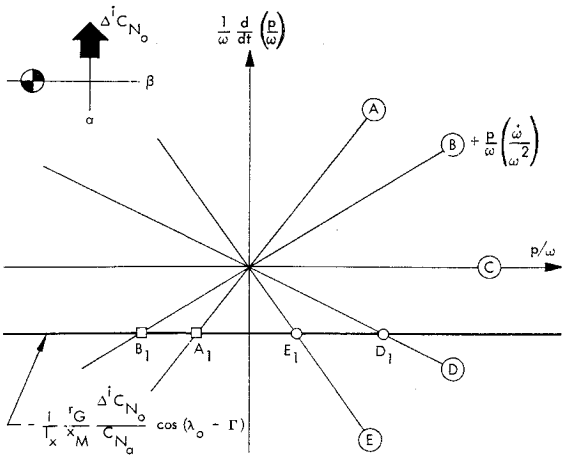

Fig. 12 Roll trim variation with environment for c.g.-$\Delta^i C_{N_o}$ coupling.

stable root no longer exists, and the roll rate will break out from resonance and continue to decrease since $d(p/\omega)/dt$ is negative. An initial spin rate will increase slightly at the small dynamic pressure but will pass through resonance before root B_1 appears. Thereafter it will decrease toward the negative stable roots and thence through D'_4 as before. With smaller asymmetry combinations, the roll rate behavior can be estimated in a similar manner.

Roll Trims with $\Delta^i C_{N_o}$

The coupling between c.g. offset and the nose asymmetry induced normal force $\Delta^i C_{N_o}$ is depicted in Fig. 12 for the maximum despin arrangement sketched in the inset. Stable roots (e.g., A_1) occur at negative roll rates which grow to infinite magnitude at peak dynamic pressure. Unstable roots (e.g., D_1) then appear at positive p/ω. Prior to peak dynamic pressure, p/ω will be driven toward negative values (i.e., despin through zero). After peak ω, p/ω can either increase or decrease, depending upon the sense of its proximity to the trim roots (e.g., to the right or left of D_1).

Since $\Delta^i C_{N_o}$ results from ablation at α_{TRIM} due to a trim asymmetry such as C_{m_o}, the combination of α_{TRIM} and $\Delta^i C_{N_o}$ coupling with c.g. offset is of more direct interest. The roll trim characteristics for the asymmetry arrangements of Figs. 10 and 12 are illustrated in Fig. 13. The (c.g. $-$ α_{TRIM}) coupling term is displaced from the abscissa by the magnitude of the (c.g. $-$ $\Delta^i C_{N_o}$) term to yield a larger despin acceleration below resonance. The previous roots near

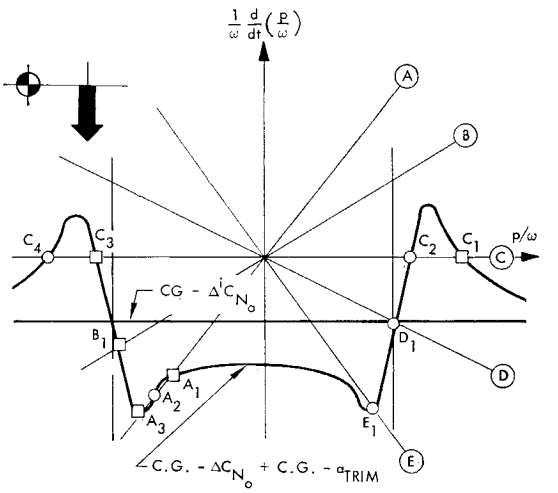

Fig. 13 Roll trims for combined c.g.-α_{TRIM} and c.g.-$\Delta^i C_{N_o}$ coupling.

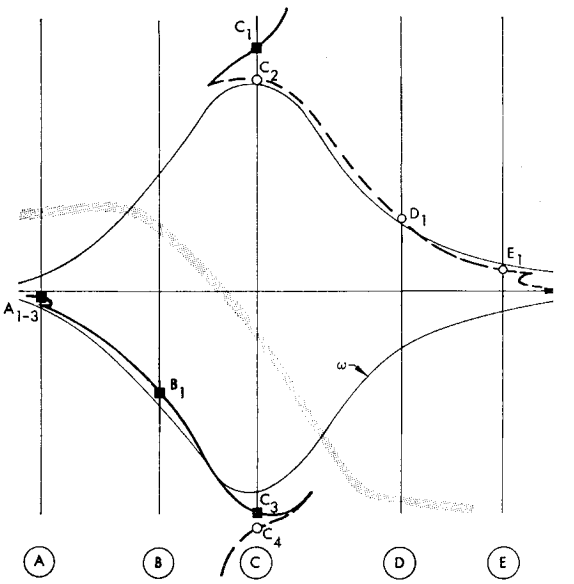

Fig. 14 Roll trim histories for combined c.g.-α_{TRIM} and c.g.-$\Delta^i C_{N_o}$ coupling.

positive resonance at time B are suppressed until time C, while roots near negative resonance now appear earlier (A_1,A_2,A_3).

The corresponding roll trim histories are shown in Fig. 14. The same general form of the contours of Fig. 11 are evident but significantly altered in time. A typical roll-rate history is traced by the shaded curve for comparison. A high rate of despin through zero occurs without roll resonance between time B and D.

Roll Trim with Ablation Grooving and Friction

In order to illustrate ablation grooving and friction effects, these terms are rewritten as

$$C_{l_o} = C_{l_f}\left(\frac{\omega d}{2V}\right)\frac{p}{\omega} + C_{l_\delta}\delta + C_{l_g}\left(\frac{\omega d}{2V}\right)\frac{p}{\omega} \qquad (7)$$

The roll trims are shown in Fig. 15 at time B only for clarity. The friction term then yields a single trim at $p = 0$ for all times in the trajectory, as would be expected. The ablation grooves act as small aspect ratio canted fins[4] to yield straight lines through the $C_{l_\delta}\delta$ ordinate at $p/\omega = 0$. It is hypothesized that the groove geometry formed at time $(t - \tau)$ persists throughout the trajectory with increasing groove depth as ablation proceeds. Hence, the fin cant angle δ will remain constant while C_{l_δ} and C_{l_g} increase in magnitude. Assuming $(t - \tau) = t_B$, the roll trims of Fig. 15 will result where root B_1 corresponds to the formation of the grooves. The stable roots approach infinite p/ω between times C and D

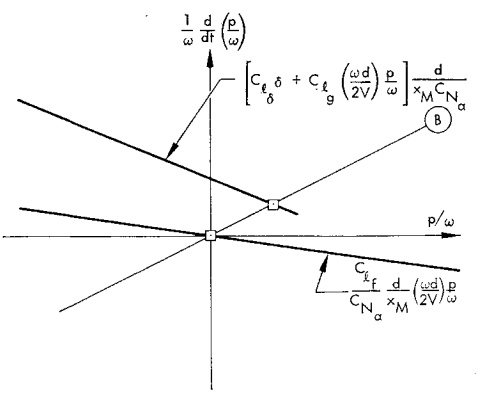

Fig. 15 Roll trim for ablation grooves and friction.

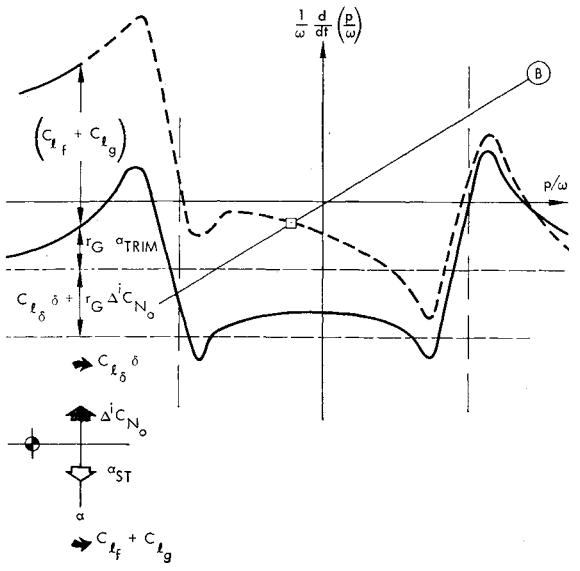

Fig. 16 Roll trim with combined asymmetries.

after which negative unstable roots appear. The steady roll rate would tend to seek the value $p/V = -C_{l_\delta}\delta/(C_{l_g}d/2)$. Hence, as velocity decreases, the spin rate would decrease proportionately. It would appear unlikely, therefore, that ablation grooving per se would cause spin reversal.

Combined Roll Trims

The individual effects of the various asymmetries can now be combined into a single diagram such as Fig. 16. The $\Delta^i C_{N_o}$ and $C_{l_\delta}\delta$ terms shift the α_{TRIM} contour vertically while the C_{l_f}- and C_{l_g}-terms tilt it. At time B, for which this figure is constructed, one negative stable root results. From similar constructions at other times of interest, the corresponding roll trim histories were obtained and are presented in Fig. 17. Note that steady roll rates in the vicinity of resonance appear at some time in the trajectory for the assumed asymmetries. A predicted roll rate history from $p_o > 0$ is included to indicate the potential despin through zero for the arrangement of asymmetries selected.

The predicted roll rate behavior for the individual terms of Eq. (3), based on the equilibrium solutions, is illustrated in Fig. 18. The spin up and despin for (c.g. $-\ \alpha_{TRIM}$) coupling is well documented in theory.[2–5] The (c.g. $-\ \Delta^i C_{N_o}$) coupling exhibits roll behavior quite similar to the (c.g. $-\ \alpha_{TRIM}$) coupling. The major difference is the lack of spin acceleration reversal during passage through resonance. The friction and groove torques will decay *toward* zero spin only.

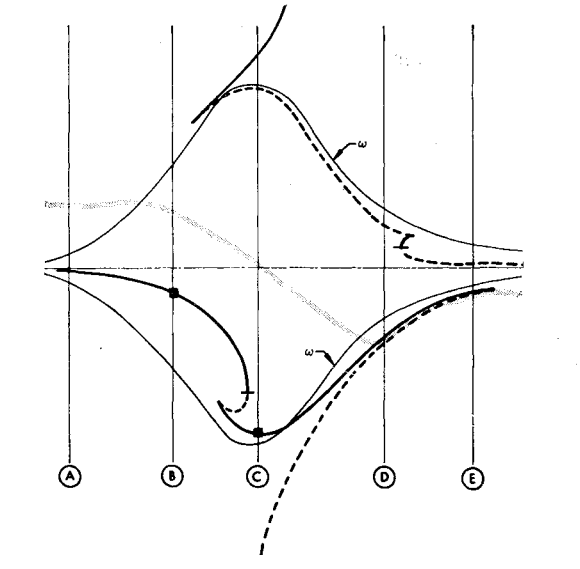

Fig. 17 Roll trim histories with combined asymmetries.

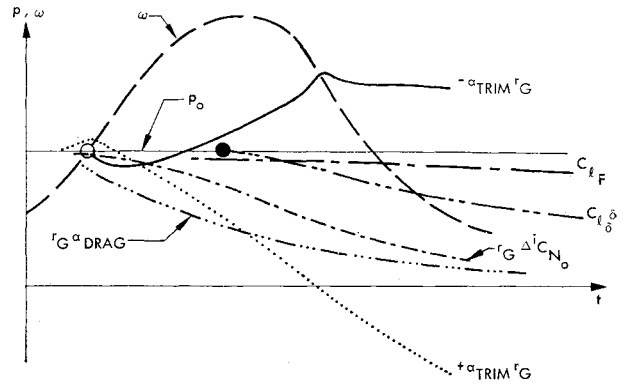

Fig. 18 Predicted roll rate histories with combined asymmetries.

Verification of the predicted roll behavior for a representative blunted cone re-entry vehicle was made with the aid of 6-degree-of-freedom digital simulations. A comparison of the effects of representative asymmetry magnitudes for (c.g. $-\ \alpha_{TRIM}$) and (c.g. $-\ \Delta^i C_{N_o}$) coupling is presented in Fig. 19.

The $\Delta^i C_{N_o}$ is seen to be equally as effective as the α_{TRIM} in changing the spin rate. The magnitude used for $\Delta^i C_{N_o}$ corresponds to 2% $\Delta r_N/r_N$ as a nose bluntness of $r_N/r_B = 0.28$ in Fig. 7. Thus, small nose asymmetries developed during flight by ablation can cause severe degradation of the spin rate control without the necessary appearance of large trim angles of attack. The effects of C_{l_f} and C_{l_δ} were examined numerically also but required inordinately large magnitudes to produce comparable spin changes.

Interpretation of Flight Data

The existence of the $\Delta^i C_{N_o}$-term will significantly affect the interpretation of flight data as shown in Fig. 20. The present interpretation of the measured normal/lateral acceleration is shown at the top. The resultant acceleration is assumed due entirely to α_{TRIM}. This can yield a misleading magnitude and orientation of the resultant trim, as illustrated in the left bottom diagram. A small $\Delta^i C_{N_o}$ out of the plane of the resultant normal force C_{N_R} will require a rotation and magnitude change of the trim component $C_{N_{TRIM}}$ for force balance. An example from the digital simulations is shown

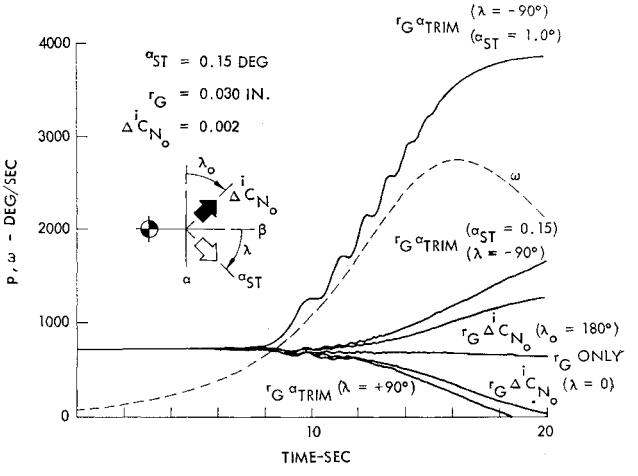

Fig. 19 Roll rate simulations.

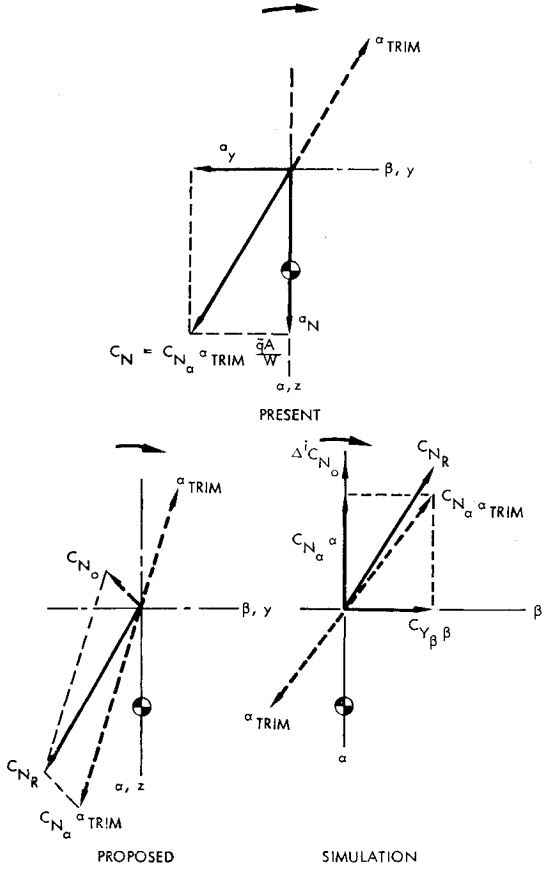

Fig. 20 Flight data interpretation.

in the right hand diagram. The α_{TRIM} orientation is displaced 4.0° from the resultant C_{NR} for a $\Delta^i C_{N_o}$ of only 0.0005 coplanar with the α_{ST}.

Conclusions

With this new source of roll torque, much of the previously unexplainable motion behavior observed in flight test appears amenable to analysis in a fairly straightforward manner. Small nose asymmetries produced by ablation at an earlier trim condition are shown to produce significant pitching moment and/or normal force increments at zero angle-of-attack, depending upon the nose bluntness. The mechanisms for coupling with lateral mass asymmetries have been described upon the basis of the equilibrium trim response in the presence of a rapidly changing environment. This previously neglected normal force component is shown to have a significant effect on interpretation of flight data.

References

[1] Nelson, R. L., "The Motions of Rolling Symmetric Vehicles Referred to the Body-Axis System," TN 3737, Nov. 1956, NACA.

[2] Glover, L., "Effects on Roll Rate of Mass and Aerodynamic Asymmetries for Ballistic Re-entry Bodies," *Journal of Spacecraft and Rockets*, Vol. 2, No. 2, March-April 1965, pp. 220–225.

[3] Pettus, J. J., "Persistent Re-entry Vehicle Roll Resonance," AIAA Paper 67-49, New York, 1966.

[4] Price, D. A., Jr., "Sources, Mechanisms, and Control of Roll Resonance Phenomena for Sounding Rockets," *Journal of Spacecraft and Rockets*, Vol. 4, No. 11, Nov. 1967, pp. 1516–1525.

[5] Mitgotsky, E., "On a Criterion for Persistent Re-Entry Vehicle Roll Resonance," AIAA Paper 67-137, New York, 1967.

[6] Seiff, A., "Secondary Flow Fields Embedded in Hypersonic Shock Layers," TND-1304, May 1962, NASA.

[7] Seiff, A. and Whiting, E. E., "Calculation of Flow Fields From Bow-Wave Profiles for the Downstream Region of Blunt-Nosed Circular Cylinders in Axial Hypersonic Flight," TND-1147, Nov. 1961, NASA.

[8] Ericsson, L. E., "Unsteady Aerodynamics of an Ablating Flared Body of Revolution Including Effect of Entropy Gradient," *AIAA Journal*, Vol. 6, No. 12, Dec. 1968, pp. 2395–2401.

[9] Ericsson, L. E. and Scholnick, I. M., "Effect of Nose Bluntness on the Hypersonic Unsteady Aerodynamics of Flared and Conical Bodies of Revolution," *Journal of Spacecraft and Rockets*, Vol. 6, No. 3, March 1969, pp. 321–324.

[10] Ericsson, L. E., "Effects of Nose Bluntness, Angle of Attack, and Oscillation Amplitude on Hypersonic Unsteady Aerodynamics of Slender Cones," AIAA Paper 70-216, New York, 1970.

[11] Ericsson, L. E. and Reding, J. P., "Ablation Effects on Vehicle Dynamics," *Journal of Spacecraft and Rockets*, Vol. 3, No. 10, Oct. 1966, pp. 1476–1483.